Coatings **2014**, *4*, 98-120; doi:10.3390/coatings4010098

OPEN ACCESS

coatings

ISSN 2079-6412

www.mdpi.com/journal/coatings

Article

Microstructural Characteristics and Tribological Behavior of HVOF-Sprayed Novel Fe-Based Alloy Coatings

Andrea Milanti [1,*], Heli Koivuluoto [1], Petri Vuoristo [1], Giovanni Bolelli [2], Francesco Bozza [2] and Luca Lusvarghi [2]

[1] Department of Materials Science, Tampere University of Technology, Tampere 33720, Finland; E-Mails: heli.koivuluoto@tut.fi (H.K.); petri.vuoristo@tut.fi (P.V.)

[2] Department of Engineering "Enzo Ferrari", University of Modena and Reggio Emilia, Modena 41122, Italy; E-Mails: giovanni.bolelli@unimore.it (G.B.); francesco.bozza@unimore.it (F.B.); luca.lusvarghi@unimore.it (L.L.)

***** Author to whom correspondence should be addressed; E-Mail: andrea.milanti@tut.fi.

Received: 13 November 2013; in revised form: 18 December 2013 / Accepted: 21 January 2014 / Published: 29 January 2014

Abstract: Thermally-sprayed Fe-based coatings have shown their potential for use in wear applications due to their good tribological properties. In addition, these kinds of coatings have other advantages, e.g., cost efficiency and positive environmental aspects. In this study, the microstructural details and tribological performances of Fe-based coatings (Fe-Cr-Ni-B-C and Fe-Cr-Ni-B-Mo-C) manufactured by High Velocity Oxygen Fuel (HVOF) thermal spray process are evaluated. Traditional Ni-based (Ni-Cr-Fe-Si-B-C) and hard-metal (WC-CoCr) coatings were chosen as references. Microstructural investigation (field-emission scanning electron microscope FESEM and X-Ray diffractometry XRD) reveals a high density and low oxide content for HVOF Fe-based coatings. Particle melting and rapid solidification resulted in a metastable austenitic phase with precipitates of mixed carbides and borides of chromium and iron which lead to remarkably high nanohardness. Tribological performances were evaluated by means of the ball on-disk dry sliding wear test, the rubber-wheel dry particle abrasion test, and the cavitation erosion wear test. A higher wear resistance validates Fe-based coatings as a future alternative to the more expensive and less environmentally friendly Ni-based alloys.

Keywords: thermal spray; HVOF; iron-based coating; microstructure; sliding wear; abrasion wear; cavitation erosion wear

---

1. Introduction

Wear is among the most serious of issues to deal with when contacting surfaces in machine parts are in relative motion, such as in bearings, joints, gears, shafts, hydraulic parts, mining industry machines, components in aeronautical industry and others. A 1997 UK industry survey estimated the cost of wear in UK industry to be about £650 million besides overhaul and machine turnover [1]. Therefore, great effort has been undertaken to minimise wear cost by design or material changes. In such a scenario, surface coating technology has gained growing interest in recent years. Among various surface coating techniques, thermal spraying has been recognized as one of the most feasible and cost-effective solutions to protect against wear and corrosion [2]. The High Velocity Oxygen Fuel (HVOF) spray process developed in the 1970s is well known as the standard technology for depositing high wear and corrosion resistant coatings. Fuel gas (propane, ethene, hydrogen) or liquid (kerosene) are mixed in a combustion chamber with oxygen at high pressure. The exhaust hot gases generated by the combustion are forced to pass through a convergent-divergent nozzle reaching supersonic velocity. Powders with typical particle sizes of 5–45 μm are axially injected into the stream of gases and dragged at supersonic velocity towards a substrate [3]. The suitable combination of moderate process temperature and high particle velocity made HVOF the standard process for manufacturing highly dense cermets coatings (e.g., WC-based and Cr_3C_2-NiCr) with excellent adhesion to the substrate and low thermal deterioration [4]. Low porosity, high hardness, high adhesion strength and compression stress are among the most important properties of HVOF-sprayed Ni-based or WC-based coatings which, in turn, comply with the requirement for high wear resistance. Nevertheless, the high and fluctuating prices of precious strategic metals such as Ni and of compounds such as WC are also driving forces for research and development to find solutions to replace such traditional coatings. Additionally, several diseases/pathologies related to nickel (pulmonary and respiratory disease—asthma, pneumoconiosis, cancer; skin diseases—eczema, allergen [5]) and WC-based materials (potential lung disease and carcinogenic agents [6]) have been recently pointed out.

Thermally sprayed Fe-based coatings have been extensively studied as a valid alternative to conventional Ni- and WC-based coatings when high anti-wear and corrosion properties are needed. The satisfactory combination of high mechanical and chemical properties, the low cost, the low environmental impact together with the health and safety make these coatings a reliable future candidate in replacing conventional thermal sprayed coatings. Excellent anti-wear and corrosion properties of Fe-based coatings were achieved by several authors [7–10]. Moreover the development of alloy compositions with high Glass Forming Ability (GFA) combined with high kinetic spraying process such as HVOF allowed for deposition of amorphous Fe-based coatings with outstanding wear resistance and corrosion properties [11,12]. Although promising results in wear and corrosion applications by using thermally sprayed Fe-based coatings have been achieved, no systematic research on relation between microstructure, mechanical properties and wear behavior of Fe-based coatings has been performed yet.

The present work focuses on the characteristics and wear properties of HVOF-sprayed Fe-Ni-Cr-B-C and Fe-Ni-Cr-Mo-B-C coatings. The chemical composition of the present Fe-based powders includes large amounts of Cr in order to form hard fine-grained precipitates, Ni to form an austenitic matrix with superior mechanical and corrosion properties compared to ferritic structure, and B as hardening

element by promoting the formation of an amorphous phase and by developing hard fine-grained precipitates [13,14]. The second composition was achieved by a customized addition of Mo in order to evaluate its effect on the properties of the resulting coatings. Several authors have reported the beneficial effect of lubricious oxides such as MoO_3 and $NiMoO_4$ on reducing the friction coefficient and, consequently, on improving sliding wear behavior [15–17]. Two conventional HVOF-sprayed Ni-based and WC-based coatings were chosen as reference. The aim of this work is to study HVOF-sprayed Fe-based coatings as a valid alternative to conventional and expensive thermally-sprayed cermet and Ni- and Co-based coatings as a wear resistant coating solution.

2. Experimental Procedure

2.1. Materials and Coating Manufacturing

Two commercially available gas atomized Fe-based powders, Fe-Ni-Cr-B-C with particle size of −45 + 15 μm and Fe-Ni-Cr-Mo-B-C with particle size of −40 + 20 μm (Wall Colmonoy Ltd., Pontardawe, UK), were employed as feedstock powders. Additionally, three powders were chosen as reference materials as representative state-of-art anti-wear coatings: agglomerated and sintered WC-CoCr (Diamalloy 5834, Sulzer Metco, Wohlen, Switzerland) with particle size of −38 + 15 μm, sintered and crushed WC-CoCr (Amdry 5843, Sulzer Metco, Wohlen, Switzerland) with particle size of −45 + 16 μm and gas atomized Ni-Cr-Fe-Si-B-C (Diamalloy 2001, Sulzer Metco, Wohlen, Switzerland) with particle size of −45 + 15 μm. The nominal chemical compositions of the powders are listed in Table 1.

Table 1. Nominal chemical composition of powders (wt%) given by supplier.

Element	Powder				
	Fe-Ni-Cr-B-C	**Fe-Ni-Cr-Mo-B-C**	**Ni-Cr-Fe-Si-B-C**	**WC-CoCr_1 (Diamalloy 5834)**	**WC-CoCr_2 (Amdry 5843)**
Fe	bal.	bal.	4	–	–
Ni	9	12	bal.	1	–
Cr	32	31	17	4	4
Mo	–	2	–	–	–
B	4	3.6	3.5	–	–
C	0.6	0.6	1	–	–
Si	–	–	4	–	–
WC	–	–	–	85	86
Co	–	–	–	10	10

Sulzer Metco Diamond-Jet Hybrid 2700 torch (Sulzer Metco, Wohlen, Switzerland) was selected to spray the powders onto low carbon steel substrates at Tampere University of Technology. Substrates were grit-blasted by using alumina grit (36 mesh) prior to spraying (grit-blasted substrate roughness $R_a = 8.3 \pm 0.9$ μm). The process parameters for the deposition of the Fe-based and of the reference coatings (WC-CoCr, Ni-Cr-Fe-Si-B-C) are presented in Table 2.

Table 2. High velocity oxygen fuel (HVOF) process parameters for the DJ Hybrid 2700 torch.

Parameters	Powder				
	Fe-Ni-Cr-B-C	**Fe-Ni-Cr-Mo-B-C**	**Ni-Cr-Fe-Si-B-C**	**WC-CoCr_1**	**WC-CoCr_2**
Air flow rate (SL/min)	375	375	375	375	375
O_2 flow rate (SL/min)	190	240	190	240	240
Propane flow rate (SL/min)	70	70	70	70	70
Powder feed rate (g/min)	60	60	60	60	60
Spray distance (mm)	230	230	230	230	230

2.2. Microstructural and Mechanical Characterization

The microstructure of the powders was investigated by Scanning Electron Microscope (SEM, Philips XL30, FEI, Eindhoven, The Netherlands) equipped with Energy Dispersive X-ray (EDX) microanalysis and their phase composition was assessed by X-Ray Diffractometry (XRD, Empyrean, PANAlytical, Cu-Kα radiation, The Netherlands). Experimental conditions include 2θ range 20–100 °, step size 0.02 °, scan speed 0.02 °/s, fixed incident beam mask 10 mm, irradiated length 5 mm, Nickel filter and PANAlytical PIXcel 3D detector. Phase identification was performed using the PANAlytical X'Pert High Score Plus software using the ICDD JCPDF-2 database (International Centre for Diffraction Data, Newtown Square, PA, USA). Particle size distribution and thermal oxidation behavior were studied by a laser diffraction method using a wet dispersion technique (Sympatec laser diffraction system) and by thermogravimetry analysis in air (TG: DTA 404, Netzsch, Selb, Germany), respectively. The microstructure of HVOF-sprayed coatings was observed by using Field-Emission Scanning Electron Microscope (FESEM, Carl Zeiss Microscopy GmbH, Germany) equipped with EDX microanalysis (INCA, Oxford instruments, High Wycombe, UK) and by XRD, under the same experimental conditions mentioned above.

Depth-sensing Berkovich micro- and nano-indentation tests (Micro-Combi tester, CSM instruments, Peseux, Switzerland) were also performed on the polished cross sections (mirror-like surface finish R_a < 0.05 μm) in order to evaluate the interlamellar and intralamellar hardness (intrinsic hardness of sprayed particle) respectively as average of 20 measurements [18]. Nano-indentations were purposely placed avoiding any particle boundaries in order to assess intralamellar hardness. Micro-indentations were performed with maximum load of 3 N, loading/unloading rate of 4.5 N/min and holding time at maximum load of 15 s. Nano-indentations were performed with maximum penetration depth of 300 nm, loading/unloading rate of 25 mN/min and holding time at maximum depth of 10 s. Nano- and Micro- Vickers hardness was calculated using the Oliver-Pharr procedure [19] in accordance with ISO 14577 standards [20]. Coating surface elasticity was estimated by the parameter $\eta_{IT} = W_{el}/W_{tot}$ defined as the ratio of the elastic work of indentation (computed as the area under the unloading part of the load-penetration curve) and the total work of indentation (area under the loading part of the curve) as shown in Figure 1.

Figure 1. Schematic representation of (**A**) indented surface and (**B**) actual load-displacement curve.

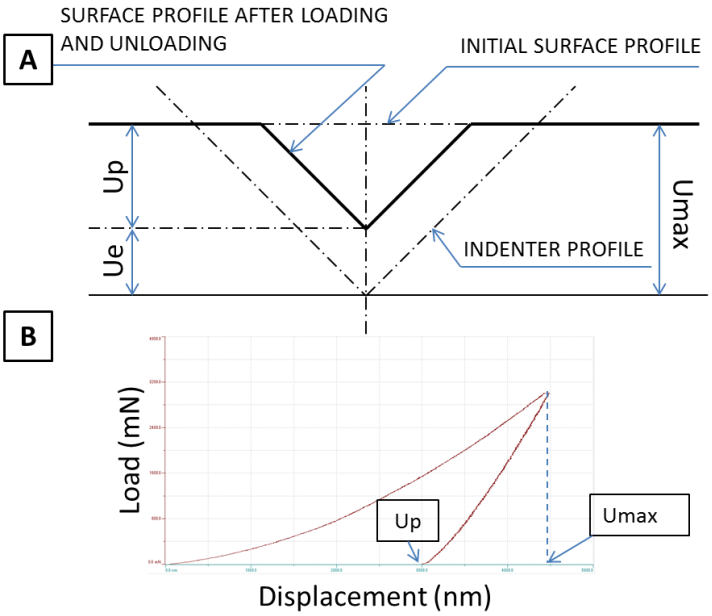

Bond strength values were determined according to the standard EN582 [21] in a tensile pull test (Instron 1185 mechanical testing machine, Norwood, MA, USA). The glue used was FM-1000 glue foil. Three measurements were carried out to calculate the average values of bond strengths. Load was measured and bond strength was calculated as load per area (diameter of the sample was 25 mm).

2.3. Wear Test

2.3.1. Dry Sliding Wear Resistance

Dry sliding wear resistance of coatings was assessed by a pin-on-disk tribometer with a ball-on-disk configuration. The sample was embedded in phenolic resin, polished up to a mirror-like surface finish (R_a < 0.05 μm) and fixed in the middle of a still table. A spherical alumina monocrystalline ball of 6.35 mm in diameter (nominal hardness ≈ 22 GPa), mounted on a rotating pin holding arm, is pressed onto the sample surface with 5 N normal load. Tests were carried out at room temperature, the wear track radius was 3.8 mm, arm the revolution speed was 150 rpm and the test lasted for 50,000 laps. The friction coefficient was continuously measured throughout the test. The wear track was measured through an optical profilometer (WYKO NT1100, Veeco, Tucson, AZ, USA) in order to calculate volume loss. The wear scars were also inspected by SEM.

Dry sliding wear rate is calculated following Equation (1):

$$K\ [\mathrm{mm^3/Nm}] = \frac{V}{w \cdot s} \quad (1)$$

where V is the volume loss (mm^3), w is the normal load (N) and s is the sliding distance (m).

Alumina counterpart wear rate was measured as well.

2.3.2. Abrasion Wear Resistance

Abrasion wear resistance was assessed by a modified version of the ASTM G65 [22] dry rubber-wheel abrasion test. Sample surfaces were ground by using 1200 grit SiC paper ($R_a \approx 8$ μm) and afterwards pressed with a normal load of 23 N against a rotating rubber wheel with a surface speed of 1.64 m/s. The test lasted for 60 min for an overall wear distance of 5904 m. Every 12 min period, the sample weight loss was measured using scales with 0.001 g accuracy and the sample position was changed to limit possible differences in wear characteristic between different positions. Dry quartz sand (SiO_2) with a grain size ranging from 0.1 to 0.6 mm was used as the abrasive. The flow rate of the abrasive was 25 g/min. The coating wear rate after a one hour test was calculated in accordance with Equation (1).

2.3.3. Cavitation Erosion Wear Resistance

Cavitation erosion wear resistance was evaluated using a vibratory apparatus according to ASTM G32 [23]. The tip of a vibrating horn, connected to a piezoelectric ultrasonic transducer, pulses in a distilled water bath at a frequency of 20 kHz with an amplitude of 50 μm. A high concentration of micrometric bubbles is produced in the fluid kept at a temperature of about 25 ℃. The bubbles impact against the sample surface, polished up to a mirror-like surface finish ($R_a < 0.05$ μm) and placed at 1 mm distance from the vibrating tip. The weight loss is periodically measured after 15 min during the first hour (in order to evaluate the incubation periods: at the very initial stage of test, material may be work-hardened and micro-cracks may form without any loss of material) and afterwards every hour up to 5 h of test. The weight loss is converted to a mean depth of erosion (MDE) following Equation (2):

$$MDE\ [\mu m] = \frac{10\Delta W}{\rho A} \quad (2)$$

where ΔW is the weight loss (mg), A is the worn area (cm^2) and ρ is the density of the material tested. Once the cavitation rate has reached a steady value, the cavitation resistance (R_e) is calculated as:

$$R_e\ [h/\mu m] = (SER)^{-1} \quad (3)$$

where SER stands for the steady erosion rate calculated as the slope of the linear fitting of MDE(t) when it becomes steady. The cavitation erosion resistance of a bulk Monel 400 alloy, generally used in maritime and hydraulic components ($\rho = 8.8\ g/cm^3$), was also assessed as a reference.

3. Results and Discussion

3.1. Microstructural Characterization of Fe-Based Powders

A spherical shape with a smooth surface and little amount of satellites was observed for both Fe-based powders (Figure 2). This is indicative of favorable fluidity during powder feeding. Fe-Ni-Cr-Mo-B-C had narrower particle size distribution (comprised within the −40 + 20 μm range) compared to Fe-Ni-Cr-B-C (comprised within the −50 + 20 μm range) (Figure 3). Both powders showed a similar thermal behavior (Figure 4). TG analysis performed in air revealed a noticeable gain of weight starting at about 1000 ℃ due to oxidation.

Figure 2. Morphology of (**A**) Fe-Ni-Cr-B-C and (**B**) Fe-Ni-Cr-Mo-B-C powders. Secondary electron SEM images.

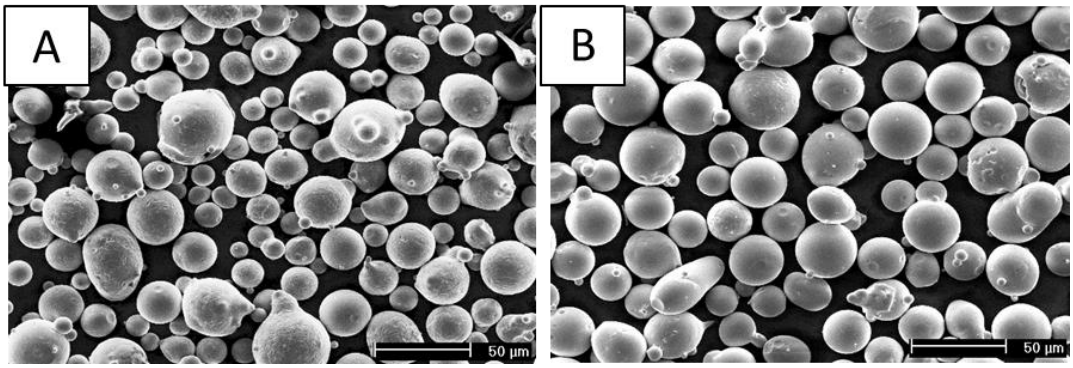

Figure 3. Particle size distributions of Fe-Ni-Cr-B-C and Fe-Ni-Cr-Mo-B-C powders. Measured by using laser diffraction.

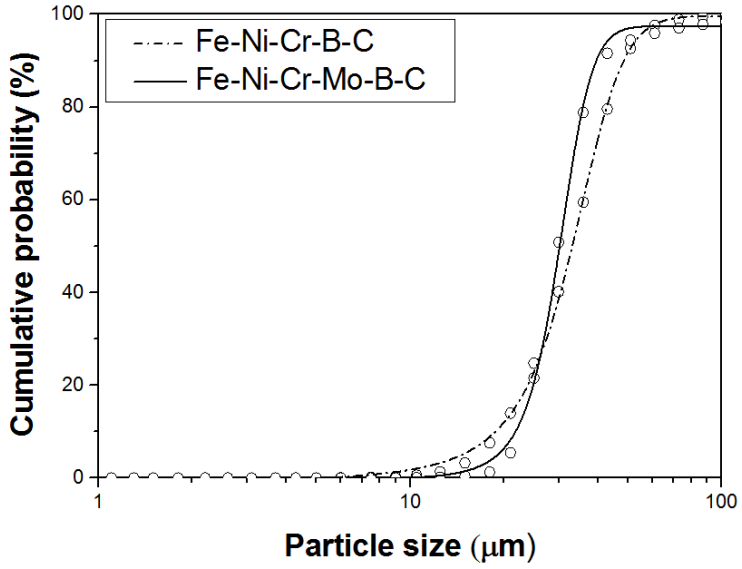

Figure 4. Thermogravimetry (TG) analysis of Fe-Ni-Cr-B-C and Fe-Ni-Cr-Mo-B-C powders.

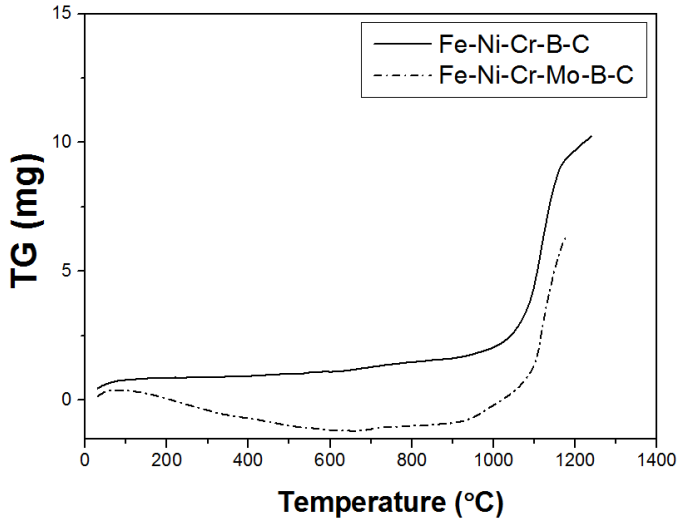

Cross-sectional SEM micrographs (Figure 5A,B) and EDS analysis (Figure 5C,D) of both powders showed heterogeneous microstructure consisting of acicular, long-shaped Cr-rich precipitates embedded and evenly distributed in a Fe-rich matrix. Cr-enriched compounds (compared to the surrounding area) are clearly shown in EDX analysis (spectra 1, 2 Figure 5C,D). XRD patterns (Figure 6) evaluation revealed the presence of austenitic (f.c.c.) ϒ matrix (JCPDS 00-03-0397) and several low intensity peaks were assigned to chromium and iron mixed carbides and borides (Cr_3C_2 03-065-2427, Cr_7C_3 01-089-5902, $(Cr,Fe)_{23}C_6$ JCPDS 01-078-1500, $(Cr,Fe)_2B$ JCPD 01-072-1073). $(Cr,Fe)_2B$, in particular, seems to be the most abundant of the secondary phases, while the other ones appear in very low amounts. Most of the acicular Cr-rich precipitates probably correspond to this phase.

Figure 5. Cross-sectional structure (Backscattered electron SEM images) and Energy Dispersive X-ray (EDX) analysis of (**A**,**C**) Fe-Ni-Cr-B-C and (**B**,**D**) Fe-Ni-Cr-Mo-B-C coatings.

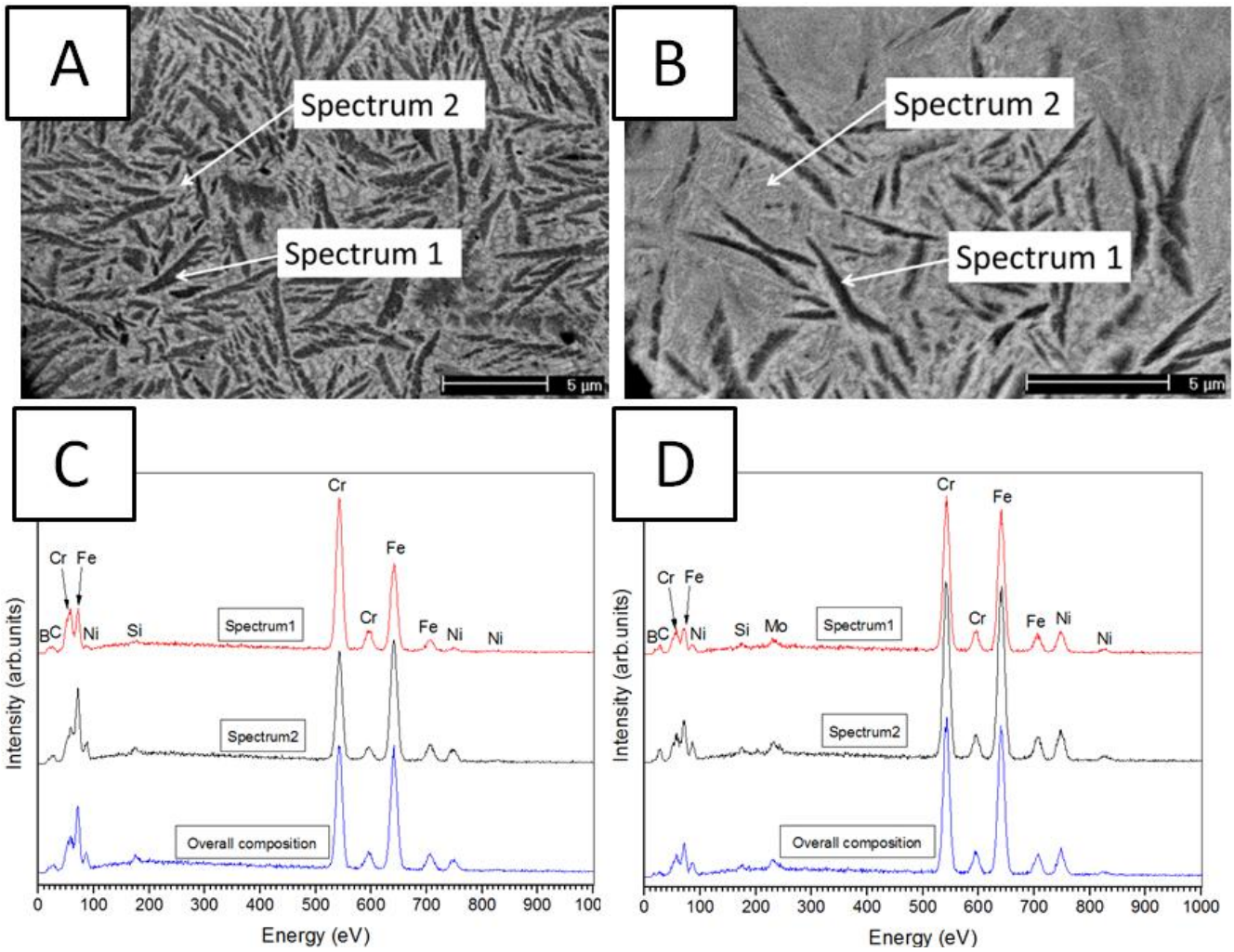

Figure 6. X-Ray diffractometry (XRD) patterns of (**A**) Fe-Ni-Cr-B-C and (**B**) Fe-Ni-Cr-Mo-B-C powders and of the respective coatings.

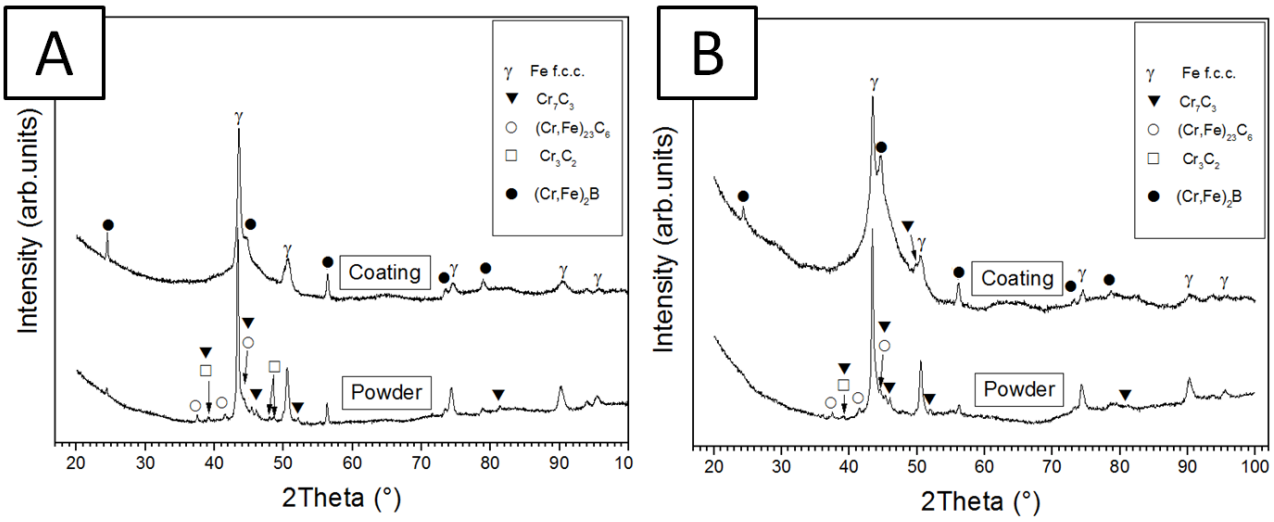

3.2. Microstructural and Mechanical Characterization of Coatings

Fe-based coatings showed quite dense microstructure (coating cross-sections in Figure 7A,B) with a calculated porosity lower than 1 vol% (image analysis) and a thickness of about 250 μm. Both microstructures were characterized by a high particle flattening ratio with some rounded particles. Remarkable microstructural differences between Fe-Ni-Cr-B-C and Fe-NiCr-Mo-B-C coatings are shown by FESEM characterization (coating cross-sections in Figure 7C,D). Fe-Ni-Cr-B-C seems to retain the microstructural details of the corresponding powder (long-shaped acicular precipitates—label "1" in Figure 7C). However, some particles (label "2" in Figure 7C) present fine-grained precipitates likely due to melting of the powder and rapid solidification in a metastable state. Conversely, the microstructure of the Fe-Ni-Cr-Mo-B-C coating showed a higher amount of particles characterized by fine-grained precipitates (label "1" in Figure 7D) and a small development of a precipitate-free particle rim which is thought to consist of a supersaturated solution and/or of an amorphous phase (label "2" in Figure 7D). Only few particles retain precipitates similar to those found in the powder (label "3" in Figure 7D). It is inferred that the Fe-Ni-Cr-Mo-B-C powder particles underwent more extensive melting, due to their narrower particle size distribution (Section 3.1) and to the warmer spraying parameters (Table 2). Therefore, during spraying, carbides and borides are thought to dissolve into the surrounding Fe-rich matrix and subsequently the rapid quenching and solidification results in precipitation of fine-grained Cr- and B-rich compounds embedded into a metastable Fe-rich solid solution which is significantly supersaturated in solute elements. A similar microstructural evolution was previously described in thermally sprayed Fe-Cr-B [24]. Feedstock powder particles consisting of boride-based phases in a Fe-based matrix were indeed also found to turn into featureless lamellae, mainly consisting of a solid solution supersaturated in boron, as a consequence of melting and impact quenching. A higher particle melting of Fe-Ni-Cr-Mo-B-C was also inferred by the lower roughness (R_a = 7.1 ± 0.5 μm) compared to Fe-Ni-Cr-B-C (R_a = 8.0 ± 0.8 μm).

Figure 7. Microstructures of High velocity oxygen fuel (HVOF) (**A**,**C**) Fe-Ni-Cr-B-C and (**B**,**D**) Fe-Ni-Cr-Mo-B-C coatings. Secondary electron FESEM images.

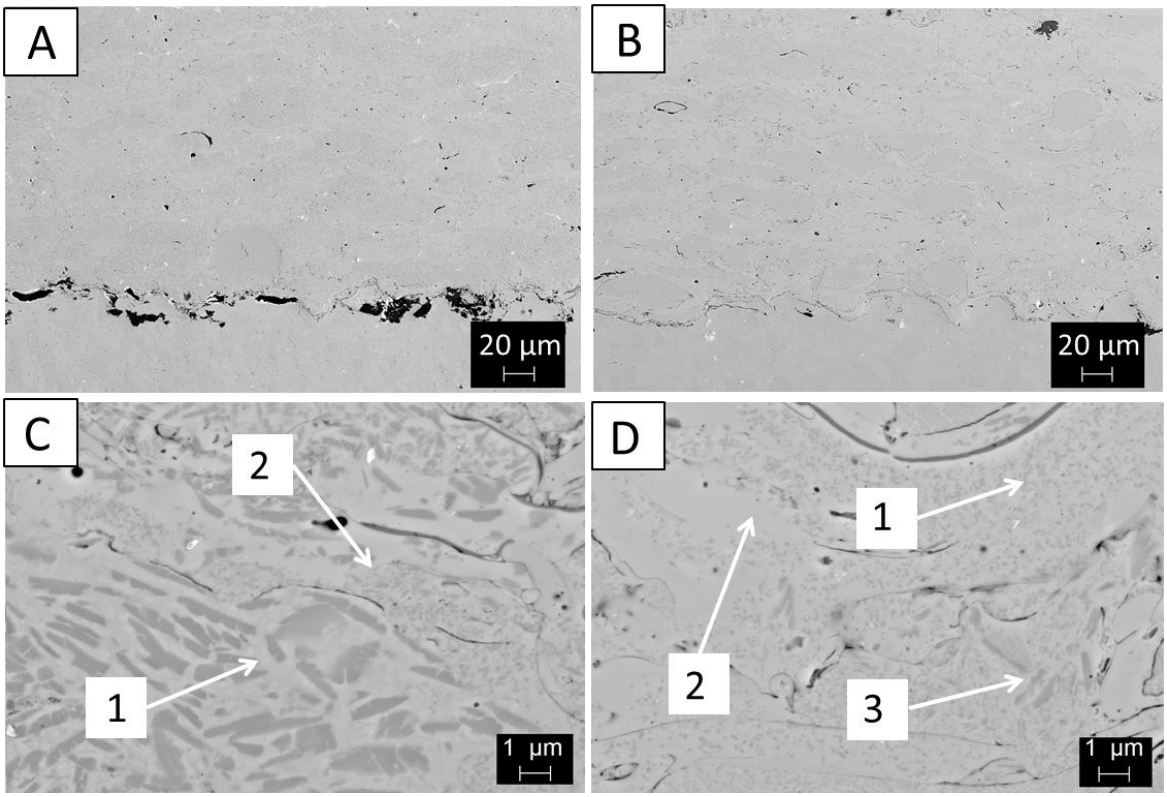

Microstructural changes were confirmed by XRD measurements (Figure 6). The main phase of both coatings was still austenitic (f.c.c.) γ-Fe (JCPDS 00-03-0397) (Figure 6A,B) with some low intensity peaks attributed to chromium and iron mixed boride $(Cr,Fe)_2B$ (JCPD 01-072-1073). Dissolution of the carbides detected in the powders and peak broadening are the results of the extensive microstructural changes occurring from powder to coatings due to the rapid quenching of molten or semi-molten particles at impact. It is worth remembering the effect of B addition. Besides the ability to form fine-grained precipitates, B (4 and 3.6 wt% in Fe-Ni-Cr-B-C and Fe-Ni-Cr-Mo-B-C, respectively) may remarkably increase the viscosity of the molten metal alloy making the melt more stable than the relative crystalline phase [25]. According to the general rules for metallic glass formation, indeed, alloys containing elements with significantly different atomic radii and large negative heats of mixing develop a viscous melt consisting of large atomic clusters, increasing the possibility to form an amorphous phase [26]. Further studies have to be done in order to assert the presence of an amorphous phase (deeper microstructural characterization has to be done, e.g., TEM).

One can clearly observe that the Fe-Ni-Cr-Mo-B-C coating underwent larger microstructural changes compared to Fe-Ni-Cr-B-C. Wider peak broadening at $2\theta \approx 43°$ and the formation of a broad band in the $35° < 2\theta < 50°$ range are observed (Figure 6B). Peak broadening is much likely due to the formation of a finely-structured supersaturated austenitic solid solution, whereas the underlying broad band probably reflects amorphous phase formation [11,12]. In the literature, similar broad bands in the diffraction patterns of thermally sprayed Fe-based alloys have indeed been univocally associated with the presence of significant amounts of amorphous phase, identified e.g., by TEM observation [14]. With regard to Fe-Ni-Cr-Mo-B-C, the narrower particle size distribution and the higher oxygen flow

rate, which in turn increases the flame temperature, provide more extensive particle heating and melting, resulting in the observed microstructural changes. Furthermore, Mo is thought to promote high viscosity at high temperature by its stabilizing effect on boride and carbides and in turn it may increase the so called Glass Forming Ability (GFA) of the sprayed alloy [27].

Besides the effect of heating and melting, it is worth mentioning that the peak broadening might be also attributed to high plastic deformation of the particles at impact. Richer *et al*. [28] reported the dissolution of β-NiAl precipitates into Co-Ni-Cr solid solution γ-matrix due to the high energy impact of particles onto the substrate during the deposition of HVOF-sprayed MCrAlY (M = Co,Ni) powders. Most likely a combined effect of melting/rapid quenching and plastic deformation of particles resulted in the dissolution of carbides and borides into the super saturated austenitic matrix. No oxide peaks are recognizable in these patterns.

The micro- and nano- hardness values of the coatings (Figure 8), assessed by depth-sensing Berkovich micro- and nano-indentation tests, are similar to those of a conventional HVOF-sprayed Ni-based alloy, with the exception of the micro-hardness of the Fe-Ni-Cr-B-C sample, which is slightly lower. The high dispersion of the results of WC-CoCr nanohardness was due to the composite microstructure of this material, with fine sized hard carbides embedded in a softer metallic CoCr binder: nanoindentation values therefore reflect the different intrinsic hardnesses of both phases. Instead the high dispersion of the results of Fe-Ni-Cr-B-C nanohardness is due to the heterogeneous microstructure as explained previously. The larger particle size distribution compared to that of Fe-Ni-Cr-Mo-B-C resulted in a less homogeneous microstructure with molten and unmolten particles with different mechanical properties. In fact, the rapid quenching of a molten particle and its solidification in a metastable state may result in greater hardness due to strengthening by solid solution as reported in another study [10]. Since nano-hardness was achieved by indentation at low penetration depth (300 nm) within the particle, it mainly reflects the intralamellar properties of the sprayed coating [29]. Instead the micro-hardness obtained at greater penetration (3 N max load) reflects the interlamellar properties [10,18]. The difference between micro- and nano-hardness is accordingly a measure of interlamellar cohesion, and it grows larger as the cohesion decreases, as shown in the literature [18,30]. It is therefore inferred that, due to the lower degree of melting of the coarser Fe-Ni-Cr-B-C powder, the interlamellar cohesion of this coating is poorer than that of the Fe-Ni-Cr-Mo-B-C coating, where the amount of fully molten particles (recognizable by their higher degree of flattening and by the presence of finer precipitates and/or of precipitate-free metastable solid solutions as described above) is higher.

Bond strengths of the coatings are shown in Table 3. HVOF-sprayed Fe-based coatings possessed bond strengths of about 30 MPa. As the failure of the WC-CoCr_2 after pull test was observed to occur in the glue, its bond strength is higher than the value reported (>64 MPa). The low in-flight oxidation and high specific weight of WC-CoCr which guarantee high kinetic particle velocity play a fundamental role in better particle sticking and in turn adhesion bond strength.

Figure 8. Berkovich micro- and nano- hardness of HVOF-sprayed coatings.

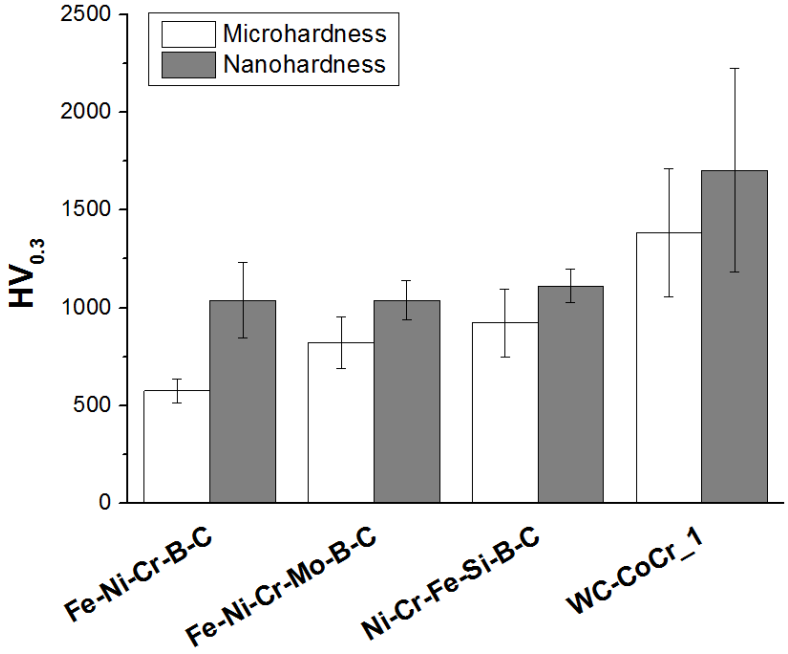

Table 3. Bond strengths and standard deviations of HVOF-sprayed coatings.

Coating	Bond strength (MPa)
Fe-Ni-Cr-B-C	31.9 ± 7.2
Fe-Ni-Cr-Mo-B-C	25.1 ± 4.5

3.3. Wear Properties

3.3.1. Dry Sliding Wear Resistance

Dry sliding wear rates (Table 4) of both Fe-based coatings were found to be lower than those of Ni-Cr-Fe-Si-B-C but still far larger than those of WC-CoCr. Wear rates of Al_2O_3 balls used against Fe-based coatings showed lower values compared to the Al_2O_3/Ni-Cr-Fe-Si-B-C coupling (Table 4). Friction coefficients of Fe-based coatings appeared lower and more stable throughout the test compared to that of Ni-Cr-Fe-Si-B-C (Figure 9). Furthermore, the Fe-Ni-Cr-Mo-B-C coating was slightly more resistant to dry sliding wear showing lower coating wear rates, lower alumina ball wear rates and a lower and more stable friction coefficient compared to Fe-Ni-Cr-B-C.

Table 4. Coating wear rates and Al_2O_3 ball counterpart wear rates after ball-on-disk.

Coating	Sample wear rate ($\times 10^{-6}$ mm^3/Nm)	Alumina ball wear rate ($\times 10^{-6}$ mm^3/Nm)
Fe-Ni-Cr-B-C	3.45 ± 0.81	0.101 ± 0.008
Fe-Ni-Cr-Mo-B-C	3.25 ± 0.44	0.095 ± 0.004
Ni-Cr-Fe-Si-B-C	8.13 ± 0.75	0.203 ± 0.037
WC-CoCr_2	0.06 ± 0.01	1.151 ± 0.131

Figure 9. Friction coefficient of HVOF-sprayed coatings against alumina ball recorded throughout the test.

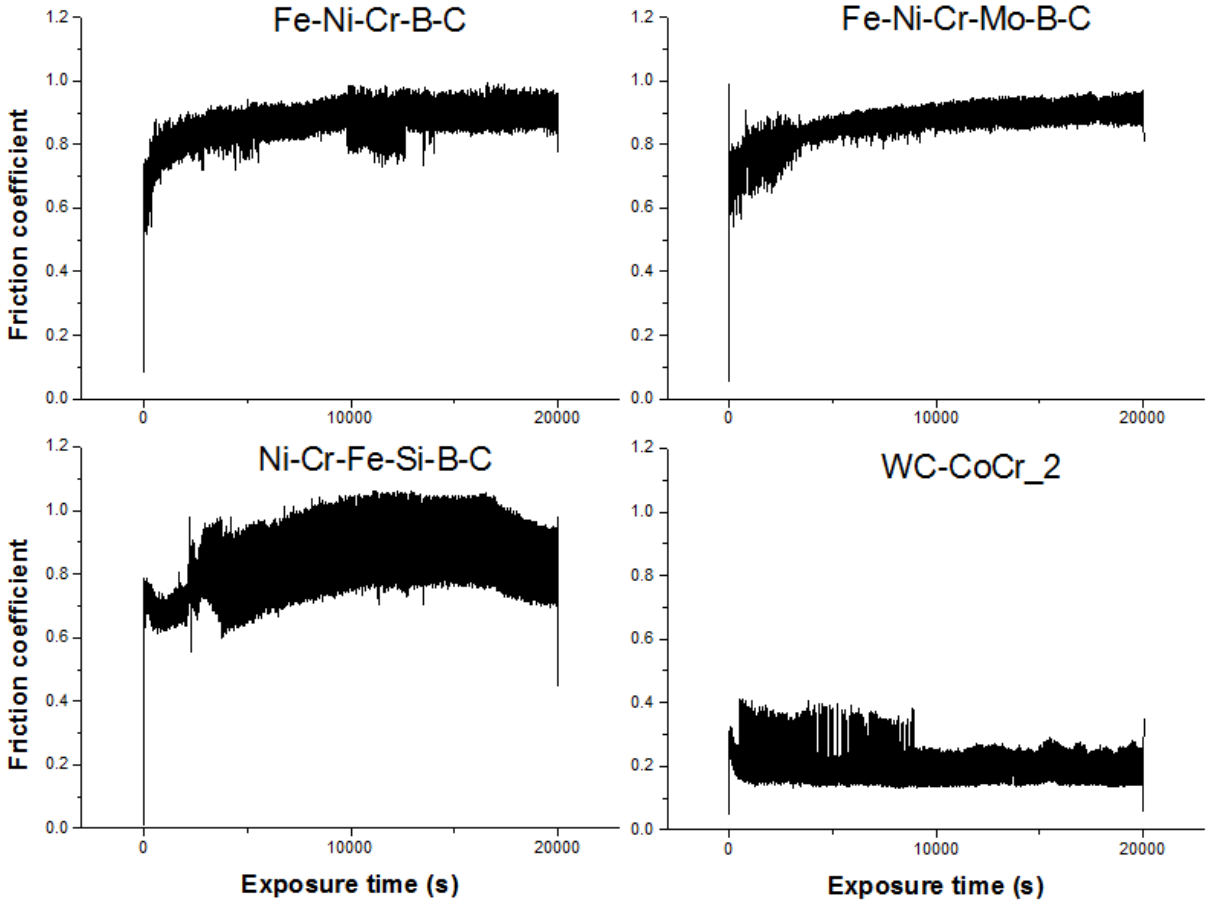

Abrasive wear occurred on both Fe-based coatings (small grooves labelled "1" in Figure 10A,B) due to the relative motion between the softer surface (Fe-based coatings) against a counterpart with harder asperities (alumina). The wear mechanism could have been worsened by the presence of hard agglomerates of oxides trapped between the mating surfaces, formed due to tribo-oxidation phenomena. Adhesive/delamination wear occurred and it was detectable by the presence of a small dark spot likely due to particle pull out (Figure 10A,B: label "2"). During the sliding test micro-welded junctions formed between the coating and the counterpart asperities. The strength of such micro-welded junctions may be greater than the bond strength between particles and this results in particle pull out. Splat delamination may also occur due to the presence of few oxide-rich intersplats which are brittle and cannot accommodate shear strains causing splat pull out [31]. These mechanisms seemed to occur more frequently on the Fe-Ni-Cr-B-C coating, consistent with the previous observations on its lower interlamellar cohesion (Section 3.2). These delaminated areas are covered up with a cluster of fine oxidized debris (spectrum 1 Figure 10C,E), further confirming the existence of triboxidative wear as well. Fe-Ni-Cr-Mo-B-C, by contrast, showed a more evenly distributed oxide layer throughout the wear track (see the dark area in the SEM-BSE inset of Figure 10B, detail in Figure 10D and EDX spectrum in Figure 10F: spectrum 1). The higher amorphous phase content of Fe-Ni-Cr-Mo-B-C coating (previously assumed) may be playing a critical role in oxidation behavior. In fact, as carbides/borides precipitate, large amounts of Cr and Mo are consumed which, in turn, causes

depletion of Cr and Mo in the surrounding area and results in a lower capability to form even and continuous oxide scale. The micro-Raman spectrum of this tribo-oxidational layer (Figure 11), characterized by a main peak at 652 cm^{-1}, accordingly confirms a significant presence of Mo. This peak is shifted to a lower wavenumber, compared to pure magnetite [32] and to the main peak in the Raman spectra of tribo-oxidational products of Fe-Ni-Cr-B-C coatings as seen in [10]. Such a shift is reportedly associated with the replacement of Fe with transition metal ions other than Ni and Cr (e.g., Mn, Cu) in the lattice of magnetite [33,34]. Although no specific study on Mo-substituted magnetite is available, the same effect is reasonably expected, leading to the conclusion that this layer contains non-negligible amounts of Mo.

Therefore, such an oxide layer could decrease the shear strength and in turn the frictional forces between the tested surface and the counterpart, reducing adhesive/delamination wear and resulting in a friction coefficient which is not only lower (Table 4), but also more stable (lower fluctuations of the friction curve in Figure 9). It is worth underlining that oxidation may be considered as a desirable event whenever a thin lubricious layer forms [35–37]. Further studies are needed to evaluate the positive effect of this oxide layer on coating wear resistance.

Figure 10. Sliding wear tracks (backscattered electron SEM images) and EDX analysis of (**A**,**C**,**E**) Fe-Ni-Cr-B-C and (**B**,**D**,**F**) Fe-Ni-Cr-Mo-B-C coatings.

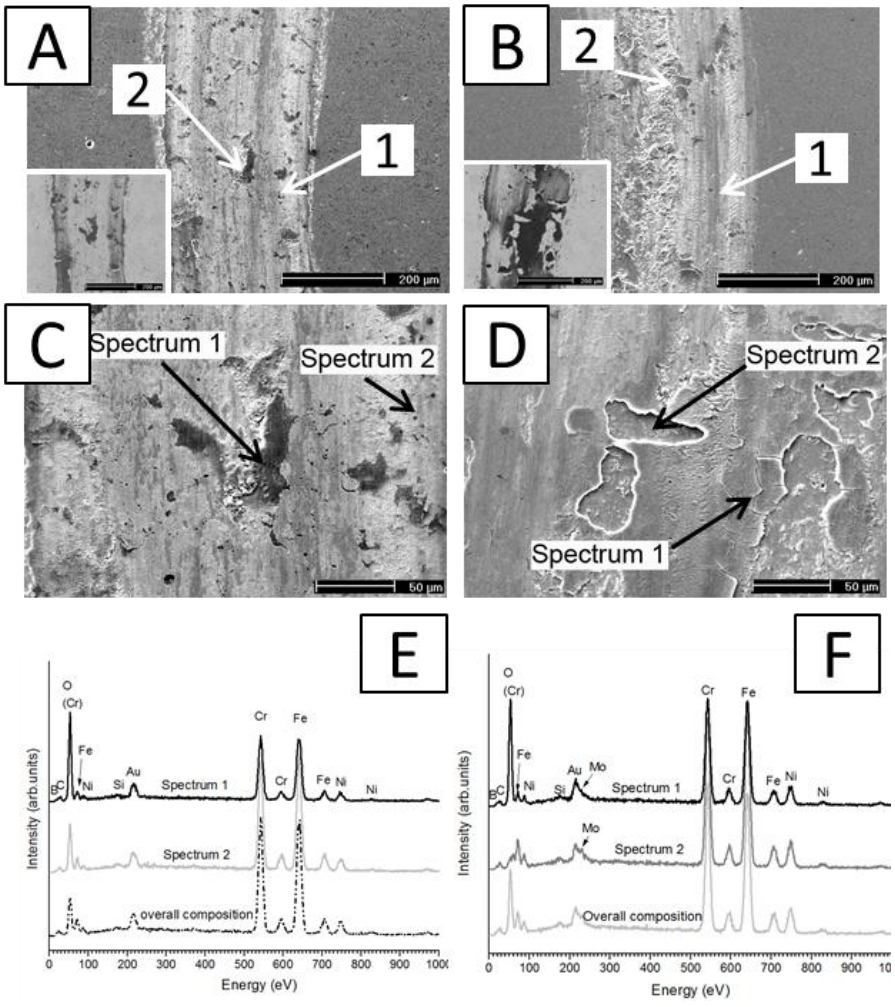

Figure 11. Micro-Raman spectrum of tribo-oxidational layer of Fe-Ni-Cr-Mo-B-C coatings.

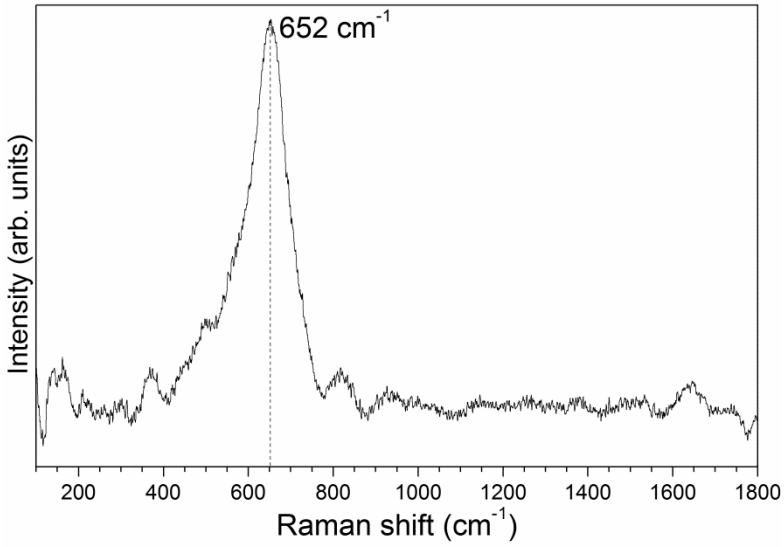

The wear track of Ni-Cr-Fe-Si-B-C presented less adhesion/delamination wear, with very limited cracking at the particle boundaries (label "1" in Figure 12A) and few delaminated particles (with fine oxides filling the resulting holes, Figure 12A—spectrum 2). Extensive triboxidation (spectrum 1, Figure 12A) and abrasion are thought to occur. The release of a larger amount of debris fragments in the contact region (due to the higher wear loss) and the instability of the oxide film, testified by the numerous delaminated areas seen in Figure 12A, probably explain the large fluctuations of the friction coefficient produced by sliding wear testing of this sample (Figure 12). Instead very shallow grooves (label "1", Figure 12B) and near-zero delaminated areas are detected on the wear track of WC-CoCr. Additionally, consistent with the high wear rate of alumina ball counterpart when testing WC-CoCr, a fine grained alumina particle area is reported (spectrum 1, Figure 12D). The lower friction coefficient of WC-CoCr may further reduce the delamination wear according to Hertzian contact theory. When two non-conformal bodies are in contact with a certain normal load combined with a tangential load (relative movements of contacting surface), the greatest value of maximum shear stress is placed below the contacting surface, at a distance which depends on the relative elastic modulus, on the radius of circular shape, and on the contacting load. As the friction coefficient increases, the maximum shear stress moves towards the surface, and it becomes located on the surface for $\mu > 0.32$ [38]. Furthermore, one can notice the high fluctuation of the WC-CoCr_2 friction coefficient within the first 9000 laps. At the very early stage of the dry sliding wear test, the hard alumina asperities may crack and get dispersed as fine wear debris between two contacting surfaces. Eventually they get stuck into the metal matrix of WC-CoCr_2 (spectrum 1, Figure 12D) resulting in a decrease of the friction coefficient (transfer mechanism, low friction coefficient alumina/alumina is well known and reported in several studies [39,40]).

Figure 12. Sliding wear track and EDX analysis of Ni-Cr-Fe-Si-B-C (**A**,**C**) and WC-CoCr_2 (**B**,**D**) coatings.

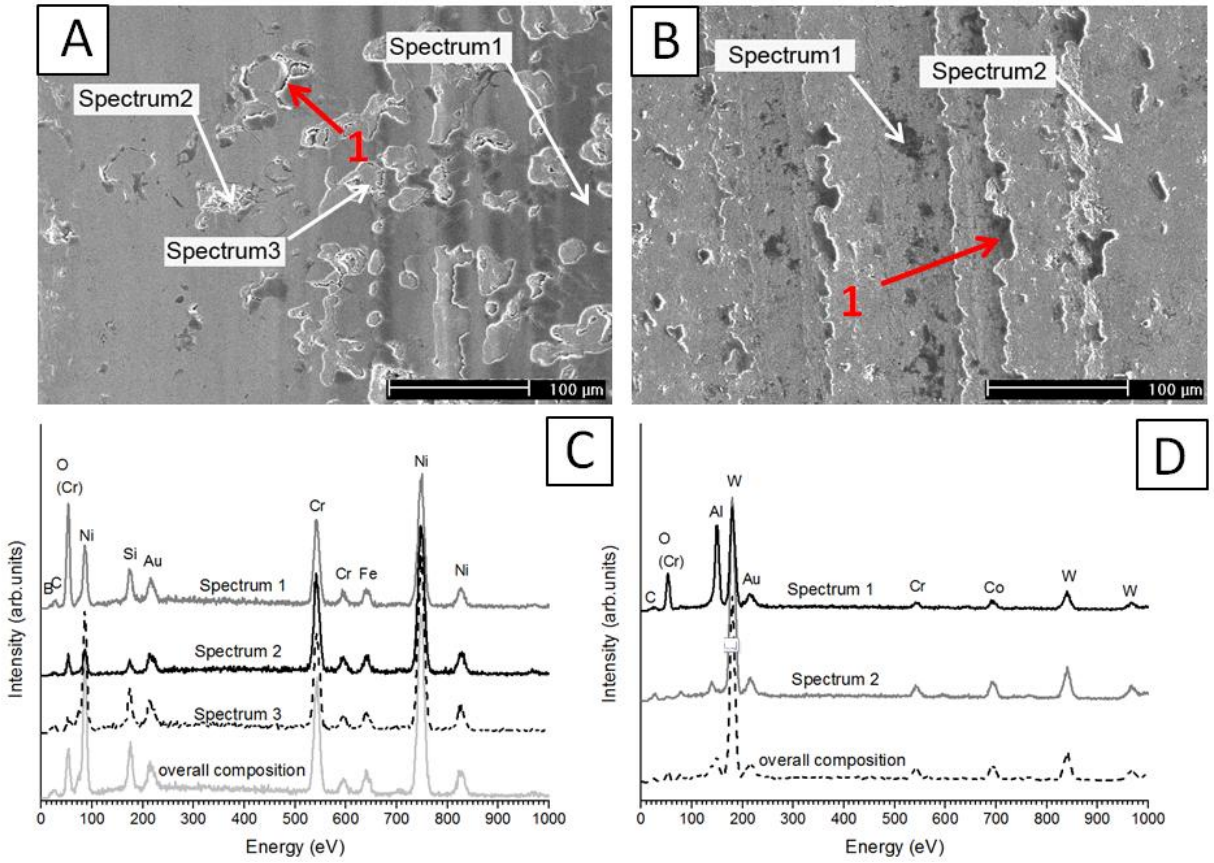

3.3.2. Cavitation Erosion Wear Resistance

The cumulative mean depth of erosion (MDE) assessed by cavitation erosion testing in distilled water is shown in Figure 13. WC-CoCr showed the highest wear resistance within the first hour (Figure 13). However, when hard carbides or particles are pulled out of the coatings, severe erosion wear and, in turn, high weight loss is created. Fe-Ni-Cr-Mo-B-C was reported to have the highest cavitation erosion resistance within 5 h (Table 5). In spite of its slightly lower adhesion strength, this sample exhibits better interparticle cohesion than the Fe-Ni-Cr-B-C coating (as witnessed by the lower difference between micro- and nano-hardness values, Section 3.2), which is particularly important for cavitation erosion resistance. In fact, in thermal spray coatings, cavitation wear generally proceeds by propagation of cracks along particle boundaries [8]. While the comparison between micro- and nano-hardness can be significant as a measure of the relative quality of interparticle cohesion, hardness, by itself, is not the most influential property controlling cavitation erosion resistance. This is witnessed by the lower erosion resistance of the hard WC-CoCr coating. Conversely, another mechanism seems to be dominant in this case. In our previous study [41], the remarkable importance of work-hardening and surface elasticity as energy dissipation mechanisms in cavitation erosion wear was discussed. Based on such results, the η_{IT} value (estimation of surface elasticity) was calculated through depth-sensing micro-indentation (Figure 14). A close correlation exists between cavitation erosion resistance and surface elasticity as a key property in order to dissipate the energy released by

bubble collapse (Figure 14). The poorer cavitation erosion resistance of Ni-Cr-Fe-Si-B-C and WC-CoCr coatings is indeed well explained by their lower surface elasticity compared to Fe-Ni-Cr-Mo-B-C. The only sample which exhibits lower cavitation erosion resistance in spite of its high elasticity is the Fe-Ni-Cr-B-C coating, on account of its lower interparticle cohesion as observed previously.

Figure 13. Variation of mean depth of erosion (MDE) of HVOF-sprayed coating samples within 5 h.

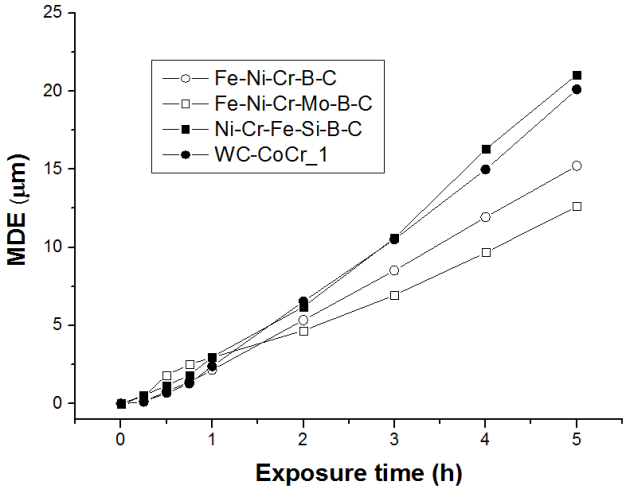

Table 5. Steady erosion rate (SER) and cavitation erosion wear resistance (R_e) of HVOF-sprayed coating samples.

Coating	SER (µm/h)	R_e (h/µm)
Fe-Ni-Cr-B-C	3.87	0.26
Fe-Ni-Cr-Mo-B-C	2.43	0.41
Ni-Cr-Fe-Si-B-C	4.62	0.22
WC-CoCr_1	4.39	0.23

Figure 14. Cavitation erosion wear resistance *vs.* estimation of surface elasticity (η_{IT}) for HVOF-sprayed coating samples.

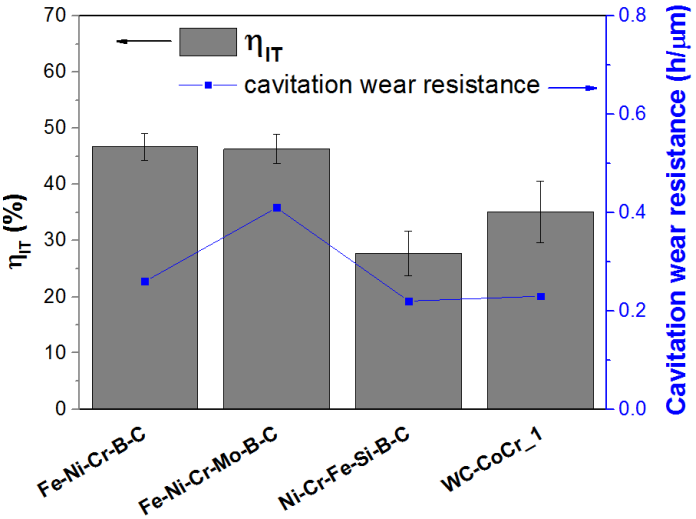

A further comparison between the best performing Fe-based coating (Fe-Ni-Cr-Mo-B-C) and bulk Monel400 alloy (Ni-30Cu), commonly used for maritime and hydraulic applications (pump shafts, seawater valves, piping system), was performed in order to validate the replacement of conventional bulk material with this promising HVOF Fe-based sprayed coating. In Figure 15, the Ni-30Cu bulk material presented an incubation period within the first hour in which the material is most likely work hardened, or cracks may form without any detectable loss of material. Afterwards, the MDE increased due to crack propagation reaching a steady state. Conversely, Fe-Ni-Cr-Mo-B-C showed higher cavitation wear rate within the first test hour most likely due to the slightly lower strength of the superficial layer of thermal spray coating compared to Monel400 alloy. Indeed, in coating deposited by high kinetic energy thermal spray processes, such as the HVOF technique, extensive deformation and densification occurs due to the "peening effect" of impinging particles that effectively hammer the previously deposited layers [42,43]. The outermost layer is therefore slightly less dense and possesses lower overall strength compared to the inner layers, as it lacks this peening effect. After removal of this superficial layer, however, the cavitation erosion rate of the coating decreased to a lower value. To sum up, the Fe-Ni-Cr-Mo-B-C coating presented a lower steady erosion rate (SER) and in turn higher cavitation wear resistance within the 5 h test.

Figure 15. Variation of mean depth of erosion (MDE) of HVOF-sprayed Fe-Ni-Cr-Mo-B-C coating and Ni-30Cu bulk material.

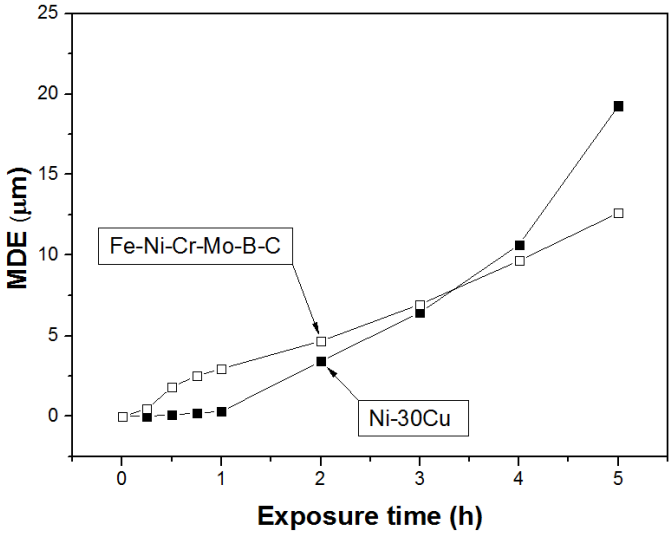

3.3.3. Abrasion Wear Resistance

Abrasion wear resistance was evaluated by the rubber-wheel test. As expected, the WC-CoCr hard metal coating showed a remarkably higher abrasion wear resistance due to its superior hardness. Hardness, which expresses the overall resistance to plastic deformation, plays a very important role in this case. However, Fe-based coatings turned out to be comparable to Ni-Cr-Fe-Si-B-C (Figure 16), or even better, when the weight loss is converted to a volumetric abrasion wear rate accounting for material density (Table 6).

Figure 16. Weight loss of tested sample recorded within a 1-h long rubber-wheel abrasion wear test.

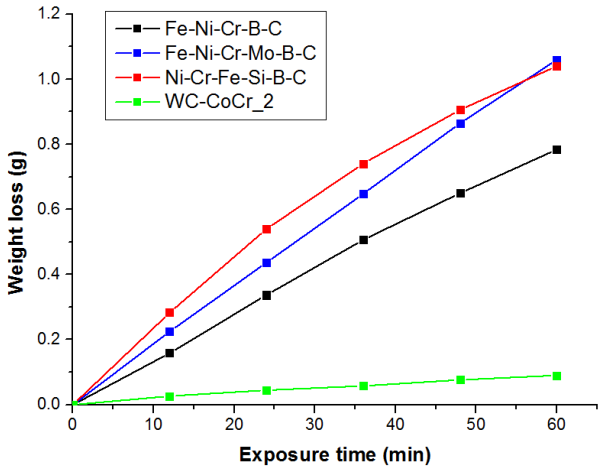

Table 6. Weight loss and abrasion wear rate for a 1-h long rubber-wheel abrasion wear test.

Measured quantity	Coating			
	Fe-Ni-Cr-B-C	**Fe-Ni-Cr-Mo-B-C**	**Ni-Cr-Fe-Si-B-C**	**WC-CoCr_2**
weight loss (mg)	784	1060	1040	90
wear rate (*10^{-5} mm^3/Nm)	74.3	100.5	112.0	4.6

4. Conclusions

This study focused on the microstructural and mechanical characterization and on the tribological behavior of novel HVOF-sprayed Fe-based coatings compared to conventional HVOF-sprayed Ni-Cr-Fe-Si-B-C and WC-CoCr coatings taken as references. Their microstructural details, micro-mechanical properties, sliding, abrasive and cavitation erosion behavior were studied and to sum up, the main conclusions are listed as follows:

- Fe-based coatings showed a dense microstructure with negligible porosity (<1% calculated through image analysis). The powder microstructure is only partly retained in the coatings after deposition. High flame temperature resulted in in-flight melting of several particles and in their deposition in the molten or semi-molten state. The rapid quenching and solidification led to precipitation of fine-grained Cr- and B-rich compounds embedded into a supersaturated Fe-rich solid solution. Higher microstructural alteration was detected in Fe-Ni-Cr-Mo-B-C due to finer particle size distribution and a warmer set of spraying parameters. No significant oxide inclusions were detected in the coatings.
- Fe-based coatings possess remarkably high nano-hardness revealing high intrinsic hardness of the sprayed material, comparable to that of Ni-Cr-Fe-Si-B-C. Moreover, considering the ratio between micro- and nano- hardness as an estimation of cohesion strength, the Fe-Ni-Cr-Mo-B-C coating was found to have similar micromechanical properties compared to a conventional HVOF-sprayed Ni-based alloy, while the Fe-Ni-Cr-B-C sample had somewhat poorer cohesion. Furthermore, Fe-based coatings possess lower bond strength compared to the reference coatings,

as evaluated by tensile testing according to the standard EN582. Bond strength is reported to be about 30 MPa.

- Although the dry sliding wear resistance of HVOF-sprayed Fe-based metal alloy coatings could not compare with that of a cermet material (WC-CoCr), their sliding wear rate was reported to be lower than that of conventional HVOF-sprayed Ni-based metal alloy coatings. Fe-based coatings are found to possess a lower and more stable friction coefficient and more specifically the formation of a Mo-containing oxide scale during sliding wear is effective in reducing adhesion to the counterbody, decreasing friction and lessening the fluctuation of the friction coefficient.
- HVOF-sprayed Fe-based coatings, but most specifically the novel composition (Fe-Ni-Cr-Mo-B-C), presented superior cavitation wear resistance in comparison to those of Ni- and WC-based conventional coatings. Its high surface elasticity, as determined by depth sensing indentation tests, coupled to its good interparticle cohesion, indicated by the relatively low difference between micro- and nano-hardness values, were found to play a fundamental role in the energy dissipation mechanism during bubble impact.
- Abrasion wear resistance of the cermet reference (WC-CoCr) is noticeably higher than that of Fe-based coatings due to higher hardness, which prevents the abrasive sand from penetrating into the coating and from ploughing out a groove by plastic deformation. However, Fe-based coatings showed lower abrasion wear rate compared to a Ni-based reference coating.

As a summary, Figure 17 shows the radar wear rates diagram of HVOF-sprayed Fe-based, Ni-based, WC-CoCr tested coatings. HVOF-sprayed Fe-based coatings represent a valid alternative to Ni-based alloys when higher anti- sliding, abrasion and cavitation wear properties are needed due to the high coating quality with acceptable micro-hardness. However, their sliding and abrasion wear resistance could not compare to that of WC-CoCr, whose superior hardness offers higher protection against scratching from hard counterparts, debris and quartz sand. Nevertheless, Fe-based coatings showed outstanding cavitation wear resistance, twice as high as that of WC-CoCr and Ni-Cr-Fe-Si-B-C coatings and even better than that of commonly used Ni-30Cu bulk material, mainly due to the higher surface elasticity.

Figure 17. Radar wear rates diagram of HVOF-sprayed Fe-based, Ni-based and WC-CoCr coatings.

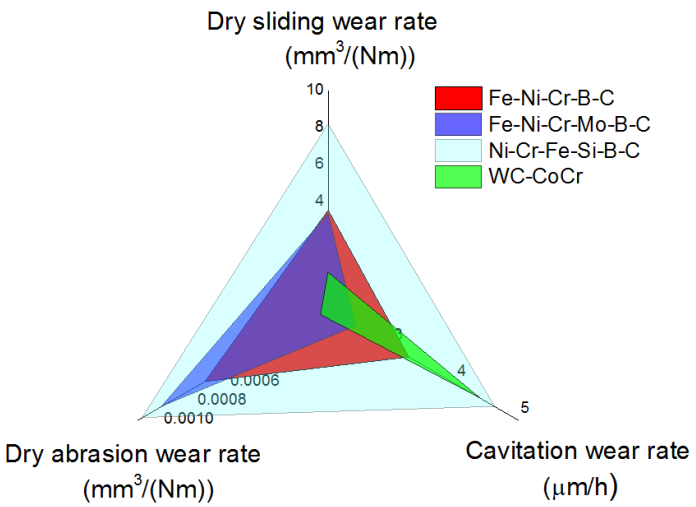

The superior surface elasticity of Fe-Cr-Ni-Mo-B-C may be due to the higher amorphous content. However further work involving deeper microstructural analysis has to be done in order to confirm the presence of amorphous phase.

Acknowledgments

The authors would like to thank Mikko Kylmälahti of Tampere University of Technology, Department of Materials Science for spraying the coatings. The study was supported by the Finnish National Graduate School (Concurrent Mechanical Engineering) and Tampere University of Technology.

Conflicts of Interest

The authors declare no conflict of interest.

References

1. Mellor, G.B. *Surface Coatings for Protection against Wear*; CRC Press: Boca Raton, FL, USA, 2006.
2. Davis, J.R. *Handbook of Thermal Spray Technology*; ASM International: Materials Park, OH, USA, 2004; pp. 171–213.
3. Pawlowski, L. *The Science and Engineering of Thermal Spray Coatings*, 2nd ed.; John Wiley & Sons: Chichester, UK, 2008.
4. Berger, L.M. Hardmetal as thermal spray coatings. *Powder Metall.* **2007**, *50*, 205–214.
5. Montavon, G. Safety Issues and Risks Related to Thermal Spray Process. ETSA Summer School Tampere University of Technology, Tampere, Finland, 13–14 June 2012.
6. *Cobalt–Tungsten Carbide: Powders and Hard Metals*; 12th Report on Carcinogens; U.S. Department of Health and Human Services: Washington, DC, USA, 10 June 2011.
7. Yuping, W.; Pinghua, L.; Chenglin, C.; Zehua, W.; Ming, C.; Junhua, H. Cavitation erosion characteristics of a Fe–Cr–Si–B–Mn coating fabricated by high velocity oxy-fuel (HVOF) thermal spray. *Mater. Lett.* **2007**, *61*, 1867–1872.
8. Schwetzke, R.; Kreye, H. *Cavitation Erosion of HVOF Coatings*; ASM International: Material Park, OH, USA, 1996.
9. Pukasiewicz, A.G.M.; Capra, A.R.; Paredes, R.S.C. Cavitation Erosion Mechanism in Fe-Mn-Cr-Si-Ni Arc Thermally Sprayed Coatings. In Proceedings of the International Thermal Spray Conference 2011, Hamburg, Germany, 27–29 September 2011.
10. Bolelli, G.; Bonferroni, B.; Laurila, J.; Lusvarghi, L.; Milanti, A.; Niemi, K.; Vuoristo, P. Micromechanical properties and sliding wear behaviour of HVOF-sprayed Fe-based alloy coatings. *Wear* **2012**, *276–277*, 29–47.
11. Cherigui, M.; Feraoun, H.I.; Feninehe, N.E.; Aourag, H.; Coddet, C. Structure of amorphous iron-based coatings processed by HVOF and APS thermally spraying. *Mater. Chem. Phys.* **2004**, *85*, 113–119.
12. Guo, R.Q.; Zhang, C.; Chen, Q.; Yang, Y.; Li, N.; Liu, L. Study of structure and corrosion resistance of Fe-based amorphous coatings prepared by HVAF and HVOF. *Corros. Sci.* **2011**, *53*, 2351–2356.

13. Kumar, S.; Kim, J.; Kim, H.; Lee, C. Phase dependence of Fe-based bulk metallic glasses on properties of thermal spray coatings. *J. Alloys Compd.* **2009**, *475*, L9–L12.
14. Chokethawai, K.; McCartney, D.G.; Shipway, P.H. Microstructure evolution and thermal stability of an Fe-based amorphous alloy powder and thermally sprayed coatings. *J. Alloys Compd.* **2009**, *480*, 351–359.
15. Shina J.H.; Wang, Q.M.; Kima, K.H. Microstructural evolution and tribological behavior of Mo–Cu–N coatings as a function of Cu content. *Mater. Chem. Phys.* **2011**, *130*, 870–879.
16. Tiana, B.; Yuea, W.; Fua, Z.; Gu, Y.; Wang, C.; Liu, J. Surface properties of Mo-implanted PVD TiN coatings using MEVVA source. *Appl. Surf. Sci.* **2013**, *280*, 482–488.
17. Woydt, M.; Skopp, A.; Dörfel, I.; Witk, K. Wear engineering oxides/anti-wear oxides. *Wear* **1998**, *218*, 84–95.
18. Nohava, J.; Bonferroni, B.; Bolelli, G.; Lusvarghi, L. Interesting aspects of indentation and scratch methods for characterization of thermally-sprayed coatings. *Surf. Coat. Technol.* **2010**, *205*, 1127–1131.
19. Archard, J.F. Contact and rubbing of flat surface. *J. Appl. Phys.* **1953**, *24*, 981–988.
20. *ISO 14577-1:2002(en): Metallic Materials—Instrumented Indentation Test for Hardness and Materials Parameters*; International Organization for Standardization: Geneva, Switzerland, 2002.
21. *EN 582:1993: Thermal Spraying. Determination of Tensile Adhesive Strength*; European Committee for Standardization: Brussels, Belgium, 1993.
22. *ASTM G65-04(2010): Standard Test Method for Measuring Abrasion Using the Dry Sand/Rubber Wheel Apparatus*; ASTM International: West Conshohocken, PA, USA, 2010.
23. *ASTM G32-10: Standard Test Method for Cavitation Erosion Using Vibratory Apparatus*; ASTM International: West Conshohocken, PA, USA, 2010.
24. Jin, H.W.; Rhyim, Y.M.; Hong, S.G.; Park, C.G. Microstructural evolution of the rapidly quenched Fe–Cr–B alloy thermal spray coatings. *Mater. Sci. Eng. A* **2001**, *304–306*, 1069–1074.
25. Wang, W.H.; Dong, C.; Shek, C.H. Bulk metallic glasses. *Mater. Sci. Eng. R* **2004**, *44*, 45–89.
26. Inoue, A. Glass-forming ability of alloys. *J. Non-Cryst. Solids* **1993**, *156–158*, 473–480.
27. Leffler, B. *STAINLESS—Stainless Steels and Their Properties*, 2nd ed.; Avesta Sheffield AB Research Foundation, Avesta Sheffield Ltd: Sheffield, UK, 1998.
28. Richer, P.; Yandouzi, M.; Beauvais, L.; Jodoin, B. Oxidation behaviour of CoNiCrAlY bond coats produced by plasma, HVOF and cold gas dynamic spraying. *Surf. Coat. Technol.* **2010**, *204*, 3962–3974.
29. Margadant, N.; Neuenschwander, J.; Stauss, S.; Kaps, H.; Kulkarni, A.; Matejicek, J.; Rössler, G. Impact of probing volume from different mechanical measurement methods on elastic properties of thermally sprayed Ni-based coatings on a mesoscopic scale. *Surf. Coat. Technol.* **2006**, *200*, 2805–2820.
30. Bolelli, G.; Rauch, J.; Cannillo, V.; Killinger, A.; Lusvarghi, L.; Gadow, R. Microstructural and tribological investigation of High-Velocity Suspension Flame Sprayed (HVSFS) Al_2O_3 coatings. *J. Therm. Spray Technol.* **2009**, *18*, 35–49.
31. Zhang, C.; Liu, L.; Chan, K.C.; Chen, Q.; Tang, C.Y. Wear behavior of HVOF-sprayed Fe-based amorphous coatings. *Intermetallics* **2012**, *29*, 80–85.

32. Shebanova, O.N.; Lazor, P. Raman spectroscopic study of magnetite ($FeFe_2O_4$): A new assignment for the vibrational spectrum. *J. Solid State Chem.* **2003**, *174*, 424–430.
33. Varshney, D.; Yogi, A. Structural and transport properties of stoichiometric and Cu^{2+}-doped magnetite: $Fe_{3-x}Cu_xO_4$. *Mater. Chem. Phys.* **2010**, *123*, 434–438.
34. Varshney, D.; Yogi, A. Structural and transport properties of stoichiometric Mn^{2+}-doped magnetite: $Fe_{3-x}Mn_xO_4$. *Mater. Chem. Phys.* **2011**, *128*, 489–494.
35. Uozato, S.; Nakata, K.; Ushio, M. Evaluation of ferrous powder thermal spray coatings on diesel engine cylinder bores. *Surf. Coat. Technol.* **2005**, *200*, 2580–2586.
36. Rabiei, A.; Mumm, D.R.; Hutchinson, J.W.; Schweinfest, R.; Rühle, M.; Evans, A.G. Microstructure, deformation and cracking characteristics of thermal spray ferrous coatings. *Mater. Sci. Eng. A* **1999**, *269*, 152–165.
37. Vetter, J.; Barbezat, G.; Crummenauer, J.; Avissar, J. Surface treatment selections for automotive applications. *Surf. Coat. Technol.* **2005**, *200*, 1962–1968.
38. Holmberg, K.; Matthews, A. *Coating Tribology: Properties, Mechanisms, Techniques and Applications in Surface Engineering*, 2nd ed.; Elsevier: Oxford, UK, 2009.
39. Saikko, V.; Pfaff, H.G. Low wear and friction in alumina/alumina total hip joints: A hip simulator study. *Acta Orthop. Scand.* **1998**, *69*, 443–448.
40. Zhou, Y.S.; Ohashi, M.; Ikeuchi, K. Start up and steady state friction of alumina against alumina. *Wear* **1997**, *210*, 112–119.
41. Milanti, A.; Koivuluoto, H.; Vuoristo, P.; Bolelli, G.; Bozza, F.; Lusvarghi, L. Wear and Corrosion Resistance of High-Velocity Oxygen-Fuel Sprayed Iron-Based Composite Coatings. In Proceedings of ASME 2013 International Mechanical Engineering Congress & Exposition, San Diego, CA, USA, 15–21 November 2013.
42. Valarezo, A.; Sampath, S. An integrated assessment of process-microstructure-property relationships for thermal-sprayed NiCr coatings. *J. Therm. Spray Technol.* **2011**, *20*, 1244–1258.
43. Barletta, M.; Bolelli, G.; Bonferroni, B.; Lusvarghi, L. Wear and corrosion behavior of HVOF-sprayed WC-CoCr coatings on Al alloys. *J. Therm. Spray Technol.* **2010**, *19*, 358–367.